

Evaluating the Performance of Empirical Models of Total Electron Density and Whistler-mode Wave Amplitude in the Earth's Inner Magnetosphere

- 1 Qianli Ma^{1,2*}, Xiangning Chu³, Donglai Ma², Sheng Huang¹, Wen Li¹, Jacob Bortnik², and
- 2 Xiao-Chen Shen¹
- 3 ¹Center for Space Physics, Boston University, Boston, MA, USA
- 4 ²Department of Atmospheric and Oceanic Sciences, University of California, Los Angeles, CA, USA
- 5 ³Laboratory for Atmospheric and Space Physics, University of Colorado Boulder, Boulder, CO, USA
- 6 * Correspondence:
- 7 Oianli Ma
- 8 qianlima@ucla.edu
- 9 **Keywords:** Empirical Model, Total Electron Density, Chorus Wave Amplitude, Hiss Wave
- 10 Amplitude, Error Metric, Radiation Belt, Space Weather Prediction

11 **Abstract (<=350 words)**

- 12 Empirical models have been previously developed using the large dataset of satellite observations to
- obtain the global distributions of total electron density and whistler-mode wave power, which are
- 14 important in modeling radiation belt dynamics. In this paper, we apply the empirical models to
- 15 construct the total electron density and the wave amplitudes of chorus and hiss, and compare them
- with the observations along Van Allen Probes orbits to evaluate the model performance. The
- empirical models are constructed using the Hp30 and SME (or SML) indices, and considering the
- plasmapause defined using the occurrence rate of high-density regions. The total electron density
- model provides an overall high correlation coefficient with observations, while large deviations are
- 20 found in the dynamic regions near the plasmapause or in the plumes. The chorus wave model
- 21 generally agrees with observations when the plasma trough region is correctly modeled and for
- 22 modest wave amplitudes of 10 100 pT. The model overestimates the wave amplitude when the
- 23 chorus is not observed or weak, and underestimates the wave amplitude when a large-amplitude
- 24 chorus is observed. Similarly, the hiss wave model has good performance inside the plasmasphere
- entrus is observed. Similarly, the most wave incidental good performance inside the plasmasphere
- 25 when modest wave amplitudes are observed. However, when the modeled plasmapause location does
- 26 not agree with the observation, the model misidentifies the chorus and hiss waves compared to
- observations, and large modeling errors occur. In addition, strong (>200 pT) hiss waves are observed
- 28 in the plumes, which are difficult to capture using the empirical model due to their transient nature
- and relatively poor sampling statistics. We also evaluate four metrics for different empirical models
- 30 parameterized by different indices. Among the tested models, the empirical model considering a
- 31 plasmapause and controlled by Hp* (the maximum Hp30 during the previous 24 h) and SME* (the
- 32 maximum SME during the previous 3 h) or Hp* and SML has the best performance with low errors
- and high correlation coefficients. Our study indicates that the empirical models are applicable for
- 34 predicting density and whistler-mode waves with modest power, but large errors could occur,
- 35 especially near the highly-dynamic plasmapause or in the plumes.

1 Introduction

- 37 The dynamic evolution of Earth's outer radiation belt electron fluxes is strongly affected by whistler-38 mode waves and the cold electron density through the wave-particle interaction processes (Thorne et 39 al., 2021). After the electrons are injected from the nightside plasma sheet, whistler-mode chorus 40 waves scatter the energetic electrons at ~1 - 100 keV energies, causing their fluxes to decay along the drift trajectory in the magnetosphere and precipitate them into the Earth's upper atmosphere (*Thorne* 41 et al., 2010; Tao et al., 2011; Ma et al., 2012). Following the commencement of geomagnetic storm 42 and the subsequent substorms, chorus waves accelerate relativistic electrons at ~100s keV - 10 MeV 43 44 energies to build up the Earth's outer radiation belt (Reeves et al., 2013; Thorne et al., 2013; Li et al., 2014; Ma et al., 2018). Hiss waves in the plasmasphere and plumes scatter the electrons at ~10 keV -45 1 MeV energies, causing the radiation belt electron flux to decay during the storm recovery phase (Ni 46 47 et al., 2013; Ma et al., 2016a). The energy-dependent slot region forms between the inner and outer radiation belts due to the dominant pitch angle scattering loss by hiss (Reeves et al., 2016; Ripoll et 48 49 al., 2016; Zhao et al., 2019). The total electron density affects the electron resonance energy due to 50 chorus and hiss waves and the efficiencies of pitch angle scattering and acceleration (Summers et al., 2007). 51
- Whistler-mode chorus waves are commonly observed in the low-density plasma trough over the nightside-dawn-dayside magnetic local time (MLT) sectors (*Li et al.*, 2009; *Meredith et al.*, 2012,
- 54 2020; Agapitov et al., 2013). Chorus waves on the nightside are strong near the equator, and the
- 55 waves on dayside have a broad latitudinal coverage with maximum power observed at off-equatorial
- 56 latitudes (*Agapitov et al.*, 2018). Chorus waves are generated by the unstable anisotropic hot
- 57 electrons injected from the nightside plasma sheet (*Li et al.*, 2008; *Fu et al.*, 2014), with wave
- intensities closely related to electron injection events (Kasahara et al., 2009; Ma, J. et al., 2022). The
- 59 statistical wave power is well correlated with the auroral electrojet index of AE or AL, which
- 60 indicates the strength of substorm injections. Chorus waves with high magnetic power are mainly
- observed to be quasi-parallel propagating. Another group of highly oblique chorus waves have high
- occurrence rates over the nightside-dawn sector close to the Earth (*Li et al.*, 2016a).
- Hiss waves are commonly observed in the high-density plasmasphere and plumes in the dayside and
- afternoon sectors (Summers et al., 2008; Li et al., 2015; Kim and Shprits, 2019; Meredith et al., 2018;
- 65 Zhang et al., 2019). The major sources of hiss include the wave amplification by anisotropic electron
- distributions in the plumes or near the outer edge of the plasmasphere (Chen et al., 2012a, 2014; Li et
- 67 al., 2013), the chorus waves propagating into the plasmasphere from the plasma trough (Bortnik et
- 68 al., 2008, 2009; Meredith et al., 2021), and the lightning generated whistlers leaking from the
- 69 ionosphere to the magnetosphere at low L shells (Sonwalkar and Inan, 1989; Bortnik et al., 2003;
- 70 Meredith et al., 2006). The statistical wave power is stronger during more disturbed geomagnetic
- 71 conditions (*Kim et al.*, 2015; *Spasojevic et al.*, 2015). The density structures in the outer
- 72 plasmasphere or plumes modulate the hiss wave intensity (Malaspina et al., 2016; Li et al., 2019; Shi
- 73 et al., 2019). In addition to the preferred wave amplification regions, the wave propagation could be
- focused, and enhanced in local high-density regions (*Chen et al.*, 2012b).
- 75 Using multiple satellite mission data in the magnetosphere, previous statistical studies have revealed
- 76 the global distribution of wave power and their dependence on geomagnetic activities. The empirical
- 77 models are widely used to construct the global wave distributions and simulate the radiation belt
- 78 electron evolution (Horne et al., 2013; Glauert et al., 2014; Drozdov et al., 2015; Ma et al., 2015).
- 79 The radiation belt simulation using empirical wave models could produce a reasonable estimate of
- 80 the electron flux decay and acceleration over a period longer than several days. However, event-
- 81 specific wave distributions from in-situ observations or other techniques are required to simulate the

- 82 dynamic electron evolution in a short timescale or during high geomagnetic activities (*Li et al.*,
- 83 2016b; *Ma et al.*, 2018).
- 84 In this paper, we evaluate the performance of empirical models of total electron density and
- amplitudes of whistler-mode chorus and hiss waves in the Earth's inner magnetosphere. Section 2
- 86 presents two events of total electron density and whistler-mode waves observed by Van Allen
- 87 Probes. Section 3 presents the empirical model based on the statistics of the Van Allen Probes
- dataset, and the data distribution comparison between observation and modeling. Section 4 compares
- 89 the performance of different models using error metrics and the Pearson correlation coefficient.
- 90 Finally, in Section 5, we summarize and discuss our results.

91 2 Van Allen Probes observation of total electron density and whistler-mode waves

- 92 We use Van Allen Probes (RBSP) measurements (Mauk et al., 2013) to obtain the total electron
- density (N_e) and whistler-mode wave amplitudes (B_w) at L < 6.5 in the Earth's inner magnetosphere.
- 94 The Electric and Magnetic Field Instrument Suite and Integrated Science (EMFISIS) measures the
- 95 DC magnetic fields and the AC signals of wave electric and magnetic fields over a broad frequency
- 96 range (*Kletzing et al.*, 2013). The background magnetic fields in three orthogonal directions are
- 97 measured by the fluxgate magnetometer. The wave electric and magnetic power spectral densities at
- 98 10 Hz 12 kHz frequencies are measured by the Waveform Receiver (WFR), which also provides the
- 99 wave polarization properties, including the wave normal angle, ellipticity, and planarity, calculated
- using the Singular Value Decomposition (SVD) method (Santolik et al., 2003). The High Frequency
- Receiver (HFR) measures the wave electric power spectral density from 10 kHz to 400 kHz,
- capturing the upper hybrid resonance band waves. The total electron density is calculated using the
- measured upper hybrid resonance frequency (*Kurth et al.*, 2015). We also use the total electron
- density inferred using the spacecraft potential measured by the Electric Field and Waves (EFW)
- instrument (Wygant et al., 2013) when the upper hybrid resonance frequency is unavailable from
- 106 HFR measurements. The density measurements from EFW have been calibrated against the more
- accurate EMFISIS density measurements (Breneman et al., 2022).
- 108 In this section, we describe the total electron density and whistler-mode wave measurements during
- two events when Van Allen Probes apogees were at different MLTs. Then, we will compare
- modeling and observation during the two events in Section 3.3.

111 **2.1 Observations on 01 March 2023**

- Figure 1 shows the total electron density and whistler-mode waves measured over a full day by Van
- Allen Probe A (panels C-F) and Probe B (panels G-J) on 01 March 2013. Figure 1A shows the
- geomagnetic Hp30 index (black) and Hp* values (blue). The Hp30 index is analogous to the Kp
- index but has a 30-min resolution (*Matzka et al.*, 2022), and we define *Hp** as the maximum *Hp30*
- index during the previous 24 h. The 24 h timescale is chosen following the plasmapause models by
- 117 Carpenter and Anderson (1992) and O'Brien and Moldwin (2003). Figure 1B shows the SuperMAG
- (Gjerloev, 2012) Auroral Electrojet index SML and the negative of SME*, where SME* is defined as
- the maximum *SME* index during the previous 3 h. A modest geomagnetic storm occurred on 01
- March 2013, as analyzed by *Ma et al.* (2016b) and *Bortnik et al.* (2018). The maximum *Hp30* index
- was close to 6, and the minimum *SML* index was about -1400 nT, indicating a disturbed geomagnetic
- 122 condition and particle injection activities.
- 123 The Van Allen Probes apogees were on the nightside (Figures 1C and 1G), suitable for measuring the
- 124 whistler-mode chorus waves during this event. The measured total electron densities (Figures 1D and

- 125 1H) show a clear plasmapause structure with a large density gradient, the separation of the dense
- 126 plasmasphere (blue) and tenuous plasma trough (black). Using the method described by Ma et al.
- 127 (2021), we identified the high-density region (blue), including the plasmasphere and plumes, and the
- low-density region (black) of the plasma trough. The density data were averaged into a 1-min time 128
- 129 cadence which is used in the statistical analysis in the following sections.
- 130 The wave magnetic power spectrograms (Figures 1E and 1I) show intense chorus waves at
- frequencies above (upper-band) and below (lower-band) $0.5 f_{ce}$, where f_{ce} is the equatorial electron 131
- gyrofrequency. The chorus waves were observed over a wide range of MLTs on the nightside. The 132
- hiss waves at frequencies from \sim 50 Hz to 1 kHz were observed mainly at L < 3.5 during this event, 133
- with weaker intensities compared to the chorus. We selected the whistler-mode wave intensities from 134
- 135 the wave power spectrograms at frequencies from 20 Hz (or the equatorial proton gyrofrequency $f_{\rm cp}$
- when $f_{cp} > 20$ Hz) to f_{ce} (or 10 kHz when $f_{ce} > 10$ kHz). In addition, we excluded the highly oblique 136
- 137 magnetosonic waves by requiring that the wave ellipticity is greater than 0.5, the wave normal angle
- 138 is below 80°, and the wave planarity is above 0.2. The chorus and hiss wave amplitudes were
- 139 calculated in both the low-density and high-density regions, respectively, as shown by the black and
- 140 blue lines in Figures 1F and 1J. During this event, the peak of chorus wave amplitude reached about
- 141 500 pT, and the hiss waves had weak amplitudes of tens of pT. We calculated the root-mean-square
- 142 (RMS) wave amplitudes during each 1-min time cadence for statistical purposes.

2.2 **Observations on 02 September 2013**

- 144 Figure 2 shows the density and waves measurements made over a full day by Van Allen Probe A
- 145 (panels C-F) and Probe B (panels G-J) on 02 September 2013. The maximum Hp30 index (Figure
- 2A) was 4, and the minimum SML index (Figure 2B) was about -900 nT, indicating a modestly 146
- 147 disturbed geomagnetic condition.

143

- 148 The Van Allen Probes apogees were located on the dusk side (Figures 2C and 2G), which is suitable
- 149 for measuring the plasmaspheric plumes and hiss waves during this event, as analyzed by Li et al.
- 150 (2019). The measured total electron densities (Figures 2D and 2H) show evident density
- 151 perturbations during each orbit of Van Allen Probes except for the Probe B observation after 16:00
- 152 UT. For example, during 13-21 UT, Figure 2D shows that Van Allen Probe A first traveled from the
- 153 plasmasphere (blue) to the plasma trough (black), encountered plumes (blue) during 16:00 - 18:30
- 154 UT, and then traveled from the plasma trough (black) back to the plasmasphere (blue). The density
- 155 measurements on different orbits suggest a highly dynamic variation of the plume on the dusk side.
- 156 Figures 2E and 2I show hiss wave activities with extended coverage in the high-density plasmasphere
- 157 and plumes. The hiss waves at frequencies of ~50 Hz - 1 kHz are correlated with the high-density
- 158 region, both during the extended plume period of 16:00 - 18:30 UT measured by Van Allen Probe A
- (Figures 2D-E) and for the short periods of density variations during 01 04 UT measured by Van 159
- 160 Allen Probe B (Figures 2I-J). The magnetosonic waves were also observed below 50 Hz during 6 - 7
- 161 UT by Probe A (Figure 2E) and during 7 - 9 UT by Probe B (Figure 2I), but they were excluded from
- our wave data using the spectral criteria described above. The chorus waves were observed in the 162
- 163 plasma trough during 19:00 - 22:30 UT by Probe B (Figure 2I). Figures 2F and 2J show that the
- 164 peaks of hiss wave amplitudes (blue) are about 100 pT both in the plasmasphere and plumes.

165 3 **Empirical model**

166

Development of the empirical model 3.1

- In previous studies, the surveys of whistler-mode chorus and hiss waves were usually modeled
- separately, and the full *L*-MLT distributions of both chorus and hiss waves were parameterized for
- different solar wind or geomagnetic conditions. However, the chorus and hiss waves are usually
- separated in space, with the chorus observed in the low-density plasma trough and the hiss observed
- in the high-density plasmasphere or plumes [e.g., Meredith et al., 2018; 2020]. Therefore, an
- additional model of the plasmapause location or plasma density is required to construct the global
- distributions of chorus and hiss using the previous models.
- We performed a survey using a unified dataset to analyze the total electron density, chorus wave
- amplitudes, and hiss wave amplitudes. This approach allowed us to construct consistent statistical
- distributions among them. Van Allen Probes measurements from September 2012 to October 2019
- were used. To obtain the global distributions, we selected data when the magnetic latitude was within
- 178 10° from the magnetic equator. The survey of total electron density was performed at $2 \le L \le 6.5$,
- 179 considering that the density at L < 2 may not be reliable when the upper hybrid resonance frequency
- is higher than 500 kHz (*Hartley et al.*, 2023). Surveys of chorus and hiss were performed at $1 \le L \le$
- 181 6.5. The whistler-mode waves at L < 2 were identified as hiss throughout our survey. The data of
- average density and root-mean-square wave amplitudes were binned in every 1 h MLT and 0.5 *L*
- 183 shell.
- We used the combination of Hp^* and SME^* (or SML) indices to categorize the statistical
- distributions of the total electron density, chorus wave amplitude, and hiss wave amplitude. The
- plasmapause location in L-MLT was previously fitted as a function of the maximum Kp index in the
- previous 24 36 h by O'Brien et al. (2003). The large amplitude chorus waves were generally found
- to be correlated with electron injections. The hiss waves are also related to the AE index, and were
- previously categorized by AE^* by Li et al. (2015). Using the combination of Hp^* and SME^* or Hp^*
- and *SML*, the model may better capture the plasmapause location and the wave activity. We set 7
- levels of Hp*(Hp*<1, 1 < Hp*<2, 2 < Hp*<3, ... <math>Hp*>6), and up to 4 levels of SME* (or SML)
- within each range of Hp^* . The ranges of SME^* (or SML) were set so that the data sample number is
- within each range of Tip. The ranges of SML (of SML) were set so that the data sample number is
- sufficient in each combination of Hp* and SME* (or SML), and the possible variation of SME* (or
- 194 *SML*) is captured.
- 195 Using the Van Allen Probes dataset, we first obtained the occurrence rates of high-density
- 196 (plasmasphere or plume) and low-density (plasma trough) flags in each L-MLT bin under each
- 197 category of *Hp** and *SME**. Then, to construct a deterministic empirical model, we set the regions
- 198 with a high-density occurrence rate higher than 0.5 to be the modeled plasmasphere or plume, and the
- regions with a low-density occurrence rate higher than 0.5 to be the modeled plasma trough.
- 200 The total electron densities with a high-density flag (blue) or a low-density flag (black) in Figures
- 201 1D, 1H, 2D, and 2H were averaged in each L-MLT bin under each combination of Hp* and SME*.
- 202 To construct the global density distribution, we used the average densities in the high-density region
- as the densities in the modeled plasmasphere or plume, and the average densities in the low-density
- region as the densities in the modeled plasma trough.
- 205 Similar to the density, we obtained the root-mean-square amplitudes of chorus and hiss waves in each
- 206 L-MLT bin under each geomagnetic condition. To construct the global distributions for a certain
- 207 geomagnetic condition, we assigned the chorus wave amplitudes in the modeled plasma trough, and
- 208 hiss wave amplitudes in the modeled plasmasphere or plume. The modeled chorus and hiss waves are
- well separated in the space. Note that the chorus and hiss waves could be modeled using different
- 210 parameters after the low- and high-density regions were modeled. For example, we used Hp* and

- 211 SML for chorus and Hp* and SME* for hiss. The model performances for different parameters are
- discussed in Section 4. The performance of the chorus wave amplitude model using Hp^* and SML is
- found to be close to the performance of the model using Hp^* and SME^* .

214 3.2 Statistical distributions

- 215 Figure 3 shows the statistical distributions of the total electron density (panels A-D), chorus wave
- amplitude (panels E-H), and hiss wave amplitude (panels I-L) for the selected Hp*, SME*, and SML
- 217 conditions. The sample numbers are shown in Figures 3M-T. The chorus waves are shown in the
- 218 modeled plasma trough region, and hiss waves are shown in the modeled plasmasphere or plume.
- During quiet times (Figures 3A, E, and I), the modeled plasmapause is mainly located at L > 6.5, and
- 220 thus the densities mainly represent the plasmaspheric density, and the hiss waves are widely
- distributed at L < 6.5, consistent with an extended plasmasphere region. As geomagnetic conditions
- become more disturbed, the total electron densities are eroded over the nightside-dawn-dayside
- sectors, showing an MLT-dependent plasmapause. The high density in the dusk sector during the
- 224 disturbed time (Figure 3D) includes the data samples of plumes or extended plasmasphere compared
- 225 to other MLTs. The chorus wave power is enhanced over the nightside-dawn-dayside sectors as the
- 226 geomagnetic activity becomes more disturbed (Figures 3F-H). Figures 3I-L show that the hiss wave
- powers are enhanced on the dayside and the dusk side at high L shells when Hp* and SME* increase,
- 228 although the overall spatial coverage becomes more limited due to the erosion of the plasmapause.
- 229 The statistical distributions of total electron density and whistler-mode waves are consistent with the
- 230 previous survey results (e.g., *Sheeley et al.*, 2001; *Li et al.*, 2009, 2015; *Meredith et al.*, 2018, 2020).
- Although the distributions under 4 conditions of Hp^* and SME^* (or SML) are shown in Figure 3, the
- empirical models cover all geomagnetic conditions and the full models are provided in the data
- 233 repository.

234

3.3 Comparison between observation and modeling during the events

- For a given value of Hp^* and SME^* (or SML) at a specific time, the empirical model provides the
- distribution of density and whistler-mode waves on a global scale by selecting data from the
- 237 corresponding geomagnetic categories. The total electron density and whistler-mode wave
- amplitudes were modeled along the L shell and MLT of Van Allen Probes from September 2012 to
- October 2019. The modeled results were produced at 2 < L < 6.5 for the density and 1 < L < 6.5 for
- 240 the wave amplitudes at a 1-min time cadence to compare with the observation. It is worth noting that
- 241 the empirical model was developed using the data samples within 10° from the equator, while the
- 242 Van Allen Probes measurements had additional sampling at latitudes up to 20°.
- Figures 1D, 1F, 1H, and 1J show the comparison between observation and modeling on 01 March
- 244 2013, when the Van Allen Probes apogees were on the nightside. The model (red) well captures the
- location of plasmapause and the density values in the plasmasphere and plasma trough (Figures 1D
- 246 and 1H). The modeling was not performed during 16:30 19:00 UT on Van Allen Probe B (Figure
- 247 1H) because the L shell was larger than 6.5. The wave mode of chorus (orange) or hiss (red) is also
- correctly identified by the model (Figures 1F and 1J). Overall, the observations of chorus (black) and
- 249 hiss (blue) show larger wave amplitude fluctuations than the modeling. The modeled chorus and hiss
- 250 waves are persistently present in the low- and high-density regions, respectively, and may not
- 251 reproduce the strong bursts or rapid disappearance of the observed waves. The large discrepancies are
- 252 found at the peak of observed wave amplitude or when the whistler-mode waves were absent, i.e., at
- 253 the extreme amplitudes. The modeling significantly overestimates the observed chorus waves during
- 254 15:00 16:30 UT observed by Probe B (Figure 1H), but the satellite was at high latitudes before

- 255 traveling towards $L \sim 7$, and the chorus waves were possibly damped in the nightside high-latitude
- 256 region.
- 257 Figures 2D, 2F, 2H, and 2J show the comparison on 02 September 2013 when the satellite apogees
- 258 were on the dusk side. Plasmaspheric plumes were observed by Van Allen Probes (blue), which were
- 259 not captured by the modeling. In Figure 2D, the modeling (red) shows the density structures of the
- 260 plasmasphere and plasma trough during 04 12 UT, and only the plasmasphere during 13 21 UT.
- 261 The modeling agrees with the observation when the high- and low-density regions are identified
- 262 correctly.
- 263 Because the high- and low-density regions are potentially mis-identified by the model, the model
- 264 predicts hiss waves when chorus waves are observed, and vice versa. The discrepancies in the wave
- amplitude modeling are larger than those in Figure 1 due to the mis-identification of the wave modes.
- For example, during 7 9 UT in Figure 2F, the observation shows that hiss $B_{\rm w} > 0$ and chorus $B_{\rm w} = 0$,
- 267 and the modeling suggests that hiss $B_{\rm w} = 0$ and chorus $B_{\rm w} > 0$. This causes an additional major source
- of modeling error, especially for the waves inside and near the plumes, in addition to the error
- sources found in Figure 1.

270 3.4 Comparision of Data Distributions from Observation and modeling

- We compare the data distribution from observations and modeling using the ~7-year dataset at 1-min
- time cadence. In this comparison and the evaluation of modeling performance discussed in Section 4,
- 273 we only used the data when the Van Allen Probes were located within 10° from the equator.
- Figures 4A, 4D, and 4G show the average total electron density, RMS amplitude of chorus, and RMS
- amplitude of hiss wave as a function of L. The observation generally agrees with the modeling
- 276 results. The high- and low-density regions were modeled using a criterion of occurrence rate at 0.5
- (see Section 3.1), causing the slight overestimate (underestimate) of chorus (hiss) B_w at L > 4.5, and
- slight underestimate (overestimate) of chorus (hiss) $B_{\rm w}$ at L < 4.5. If the average density and RMS $B_{\rm w}$
- were weighted by the occurrence rates of high- and low-density regions in the models, the modeling
- 280 would perfectly match the observation. However, such a model would not be very useful because it
- 281 mixes the plasmasphere and plasma trough densities, and the modeled chorus and hiss waves appear
- 282 simultaneously.
- 283 Figure 4B shows the probability density function (PDF) between the modeled and observed total
- electron densities. Most of the data are distributed around the diagonal line, suggesting a good model
- performance. The overall Pearson correlation coefficient (R) is 0.89. To examine the modeled data
- distribution for a fixed observation, Figure 4C shows the PDF divided by the sum of probability
- density in each range of observed N_e , denoted as the normalized PDF. The total normalized PDF for
- each range of observation is 1, so the good model will show a normalized PDF of ~0.5 1 along the
- 289 diagonal line. Figure 4c indicates good model performance when the observed density is higher than
- 290 100 cm⁻³. The modeled data shows a wide spread for the observed densities from 10 cm⁻³ to 100 cm⁻³,
- suggesting a large deviation at and near the plasmapause or plumes. For the observed densities below
- 292 10 cm⁻³, the modeled density is mainly at 3 10 cm⁻³, suggesting that the model correctly identifies
- the low-density region of the plasma trough, but the modeled density is overall higher than the
- 294 observation when the observed density is below 3 cm⁻³.
- 295 Figure 4E shows the probability density function for chorus waves. The modeled and observed
- 296 chorus waves with 0 pT amplitude, including the high-density region data (chorus $B_{\rm w}=0$) in the
- 297 modeling and observation, are included at $B_{\rm w}$ < 2 pT bins, and considered when evaluating the model

298 performance. The high PDF at observed $B_{\rm w} < 2$ pT and modeled $B_{\rm w} < 2$ pT suggests that the majority 299 of the plasmasphere regions are correctly modeled. A second group of data are found at observed 300 $B_{\rm w} > 2$ pT and modeled $B_{\rm w} < 2$ pT, representing the times when the satellite was outside the 301 plasmapause and observed chorus wave activity while the model suggests a high-density region. 302 Similarly, the group of data at observed $B_{\rm w} < 2$ pT and modeled $B_{\rm w} > 2$ pT represents the times when 303 the satellite was inside the plasmapause or chorus was not observed outside the plasmapause, while 304 the model suggests a low-density region with chorus wave activity. Figure 4F shows the normalized PDF for each range of observed chorus $B_{\rm w}$. The model underestimates the strong chorus wave 305 amplitudes for observed $B_{\rm w} > 100$ pT; specifically, the model most likely predicts a wave amplitude 306 307 of 100 - 200 pT for the observed wave amplitude of 500 - 1000 pT. The model provides a good 308 estimate of the chorus wave amplitude for the observed chorus B_w from 10 pT to 100 pT. For the 309 weak chorus waves with $B_{\rm w}$ < 10 pT, the model most likely overestimates the observation with 310 modeled $B_{\rm w}$ of 10 - 20 pT. The overall Pearson correlation coefficient for chorus $B_{\rm w}$ is 0.67, which is lower than that of the density model. The correlation coefficient is affected by the groups of data at 311 312 observed $B_{\rm w} > 2$ pT and modeled $B_{\rm w} < 2$ pT, and at observed $B_{\rm w} < 2$ pT and modeled $B_{\rm w} > 2$ pT; i.e., 313 the R is strongly affected by the mis-identification of the plasmasphere or plasma trough.

314 Figure 4H shows the probability density function for hiss. The data distribution and scattering are 315 similar to those of the chorus waves, while the amplitudes of observed and modeled hiss waves are 316 overall lower than those of chorus. The group of data at observed $B_{\rm w} > 2~{\rm pT}$ and modeled $B_{\rm w} < 2~{\rm pT}$ 317 represents the times when the spacecraft was in the high-density region and the model suggests a 318 low-density region. The data group at observed $B_{\rm w} < 2$ pT and modeled $B_{\rm w} > 2$ pT represents the 319 times when the spacecraft was in the low-density region or hiss was not observed, while the model 320 suggests hiss wave activity in a high-density region. The normalized PDF distribution (Figure 4I) suggests that the modeling agrees with observation for observed $B_{\rm w}$ from 10 pT to 50 pT, 321 322 underestimates for observed $B_{\rm w} > 50$ pT, and overestimates for observed $B_{\rm w} < 10$ pT. In addition, 323 another evident group of data is found for observed $B_{\rm w} > 200~{\rm pT}$ and modeled $B_{\rm w} < 2~{\rm pT}$ in Figure 4I. 324 The very large amplitude hiss waves, despite their overall low occurrence, are usually observed with 325 large density variations or in the plumes (Shi et al., 2019). The empirical model may not fully capture 326 the density variations, plume structures, or their evolution. Instead, these regions are likely mis-327 identified as the low-density plasma trough by the model, since the L shell of the perturbed density is 328 usually high, and the geomagnetic condition is usually disturbed (Shi et al., 2019). As a result, the 329 empirical model cannot capture the very large amplitude hiss waves. The Pearson correlation 330 coefficient for hiss is 0.53, which is lower than that of chorus.

4 Performance of different models

331

332

Metrics for evaluating the model performance 4.1

- 333 We further evaluate the model performances using various error metrics and correlation coefficients
- for different L shells. In each L shell bin, we consider the data in the range $\Delta L = \pm 0.25$. Following 334
- 335 Morley et al. (2018), we consider Mean Absolute Error (MAE), Root Mean Square Error (RMSE),
- Median Symmetric Accuracy (MSA), and Pearson correlation coefficient. Below we define x as the 336
- 337 observed N_e or B_w and v as the modeled N_e or B_w .
- 338 We calculate Mean Absolute Error normalized by the average of N_e or RMS of B_w as

339
$$MAE/Mean = \overline{|y - x|}/\overline{x} \quad \text{for } N_e,$$
340
$$MAE/RMS = \overline{|y - x|}/\sqrt{\overline{x^2}} \quad \text{for } B_w.$$
 (1)

$$MAE/RMS = \overline{|y - x|}/\sqrt{x^2} \quad \text{for } B_{\text{w}}. \tag{2}$$

341 The Root Mean Square Error normalized by the average of N_e or RMS of B_w is calculated as

342
$$RMSE/Mean = \sqrt{\overline{(y-x)^2}/\overline{x}} \quad \text{for } N_e,$$

$$RMSE/RMS = \sqrt{\overline{(y-x)^2}/\sqrt{\overline{x^2}}} \quad \text{for } B_w.$$
(4)

$$RMSE/RMS = \sqrt{(y-x)^2}/\sqrt{\overline{x^2}} \qquad \text{for } B_{\text{w}}. \tag{4}$$

344 The Median Symmetric Accuracy is calculated as

345
$$MSA = 100\left(e^{Median\left(\left|\ln\frac{y}{x}\right|\right)} - 1\right) \quad \text{for } N_e \text{ and } B_w. \tag{5}$$

The Pearson correlation coefficient is calculated as 346

$$R = \frac{\sum (x - \overline{x})(y - \overline{y})}{\sqrt{\sum (x - \overline{x})^2 (y - \overline{y})^2}} \quad \text{for } N_e \text{ and } B_w.$$
 (6)

- 348 All data, including the observed or modeled $B_{\rm w}=0$, are considered in Equations (1 - 4) and (6). To
- calculate MSA in Equation (5), the logarithm function is used, so we consider all density data, and 349
- 350 only the wave amplitude data with observed and modeled $B_{\rm w} > 10$ pT. The good model is evaluated
- 351 as having low MAE, low RMSE, low MSA, and high R.
- Although the MSA cannot be calculated for $B_{\rm w}=0$, it provides a symmetric error for underestimate 352
- and overestimate in terms of the multiplication factor, while MAE and RMSE provide symmetric 353
- errors in terms of the pencentage relative to the observation. For example, if v = 0.5x, then MAE =354
- 0.5, RMSE = 0.5, MSA = 100; if y = 2x, then MAE = 1, RMSE = 1, MSA = 1 (same as for y = 1) 355
- 0.5x); if y = 1.5x, then MAE = 0.5 (same as for y = 0.5x), RMSE = 0.5 (same as for y = 0.5x) 356
- 0.5x), MSA = 50. 357

358 4.2 Comparing different models

- 359 We evaluate the performances of 6 models categorized by different combinations of Hp30 or Hp*,
- 360 and SML or SME* indices, and the incorporation of the plasmapause. For each model, the surveys of
- 361 total electron density, chorus wave amplitude, and hiss wave amplitude are performed using the same
- combination of geomagnetic indices. The statistical methods are the same as those described in 362
- 363 Section 3 except for those described below. We perform the surveys of density and wave amplitudes
- 364 using
- 365 Empirical model 1: use Hp30 and SML indices, and consider the low- and high-density 366 categorizations in the models (same as the density categorization method described in Section 367 3.1, and denoted as 'PP');
- Empirical model 2: use *Hp30* index, and consider the low- and high-density categorizations; 368
- 369 Empirical model 3: we perform the surveys of density and wave amplitudes using SML index, 370 and consider the low- and high-density categorizations;
- Empirical model 4: use Hp* and SML indices, and consider the low- and high-density 371 372 categorizations;
- Empirical model 5: use Hp* and SME* indices, and consider the low- and high-density 373 374 categorizations;

- Empirical model 6: use Hp^* and SME^* indices; the low- and high-density categorization is not considered, but the model adopts the averages over both low- and high-density conditions weighted by their occurrence rates (denoted as 'No PP').
- 378 Models 1 3 only use the instantaneous geomagnetic conditions, and models 4 6 also consider the
- most disturbed *Hp* condition in the past 24 h. Model 6 is equivalent to the method of directly using
- 380 the models of density, chorus, and hiss waves without imposing a plasmapause. The density and
- wave models are not coupled, the plasmaspheric density could be mixed with the plasma trough
- density, and the chorus and hiss wave could appear simultaneously in the same location.
- Figure 5 shows the metrics for different models as a function of the L shell. For the total electron
- density (Figures 5A-D), models 4 and 5 using Hp* have lower MAE, lower RMSE, lower MSA and
- 385 higher R, than models 1, 2 and 3 using the Hp30 index. Although model 6 has a slightly lower RMSE
- and higher *R* than models 4 and 5, the MSA of model 6 is much higher than that of models 4 and 5.
- The best density model is model 5 using Hp^* , SME^* , and PP, with slightly lower errors and a higher
- 388 correlation coefficient than model 4. Note that the R for the density data in each L shell bin is much
- lower than the overall R for all L shells (0.89 in Figure 4B). This is because the total electron density
- 390 has a persistent L-dependence with high densities generally at low L shells, contributing to the high
- 391 correlation coefficient when the data at different L shells are included in the R calculation.
- For the chorus $B_{\rm w}$ (Figures 5E-H), models 4 and 5 have slightly lower MAE and RMSE and slightly
- higher R at L < 4 than models 1, 2, and 3, and the improvement evaluated using MSA is significant.
- 394 Although model 6 shows the lowest RMSE and MSA at L > 3.5, it has the lowest R overall and
- 395 significantly large MAE at L < 4. The best chorus wave models are 4 and 5 considering Hp^* , SML
- 396 (or *SME**), and PP, and the *R* of model 4 is slightly higher than model 5.
- For the hiss $B_{\rm w}$ (Figures 5I-L), models 4 and 5 have slightly lower RMSE and MSA than models 1, 2,
- and 3, and noticeable improvement evaluated using MAE and R. Compared to models 4 and 5, model
- 399 6 shows large MAE at L > 4 and low R at 4 < L < 6, and the performances at other regions or for
- other metrics are similar. The best model for hiss is model 5 considering Hp*, SME*, and PP, with
- 401 higher R than model 4.

- 402 The overall metrics for different models of density, chorus $B_{\rm w}$ and hiss $B_{\rm w}$ are also tabulated in Table
- 403 1, considering the data at all different L shells. Similar to the discussions above, the overall best
- 404 model is model 4 for the density and hiss and model 5 for chorus, while their performance difference
- 405 is very small. Significant modeling improvement is obtained using the Hp* index compared to the
- 406 *Hp30* index, and considering the low- and high-density categorization in the model.

5 Conclusions and discussions

- 408 We evaluated the performance of a number of empirical models describing the total electron density
- and whistler-mode wave amplitudes in the Earth's inner magnetosphere. The empirical models of
- 410 density, chorus, and hiss waves were developed using the ~7 years of Van Allen Probes data,
- 411 categorized using Hp30, SME, SML indices, and their past maximum values, with a classification of
- 412 high- or low-density regions (i.e., plasmasphere, plume or plasma trough). The models were used to
- 413 reproduce the density and wave amplitudes along the Van Allen Probes trajectories, and the data
- 414 distribution was compared between the observation and modeling results. We further used 4 metrics
- 415 to compare the performances of 6 different models, categorized using different geomagnetic indices
- or excluding the density region classification. Our model performance evaluation indicates that:

- Incorporating the plasmapause (i.e., classifying the high- and low-density regions) significantly improves the modeling of total electron density as well as the amplitudes of chorus and hiss waves.
- Using the maximum values of geomagnetic indices during the past 3 for SME and 24 h for Hp30 improves the modeling results compared to using only the instantaneous indices.
- The total electron density is well-modeled with high Pearson correlation coefficients using geomagnetic indices. The model agrees with the observation when the observed $N_e > 3$ cm⁻³ and overestimates for smaller density observations. The additional errors are near the plasmapause or in the plumes, causing the large data spread in the probability density function distribution.
- The amplitudes of whistler-mode chorus and hiss waves are well-modeled when the observed wave amplitudes are moderate, with amplitudes between 10-100 pT.
- For the observed amplitude $B_w < 10$ pT or in the absence of whistler-mode waves, the chorus and hiss models tend to provide the average wave amplitudes, which overestimate the observation.
- The models underestimate the whistler-mode wave amplitudes when the observed amplitude is intense, with values larger than 100 pT.
- The mis-identification of the plume region or the errors in identifying the plasmapause boundary causes large errors in modeling chorus and hiss wave amplitudes, because the chorus and hiss waves are mis-labeled by the model.
- The empirical model cannot capture the very large amplitude (> 200 pT) hiss waves, probably because these hiss waves are present in the plume region at high *L* shells during disturbed conditions, which is identified as the plasma trough by the model.
- To investigate the model performance properly, it is necessary to evaluate multiple error metrics and correlation coefficients. Using a single metric may provide a biased judgment for the model comparison.
- 441 Although we evaluated the performances of 6 different models, the chosen 'best' model is not yet
- optimized. For example, our model comparison mainly focused on the *Hp30* and *SME* (or *SML*)
- 443 indices and their derivatives, while the impacts of other geomagnetic indices and solar wind
- parameters have not been investigated. The solar wind dynamic pressure may significantly impact the
- 445 whistler-mode waves at L > 6 due to the compression of the magnetosphere (Yue et al., 2017; Zhou et
- 446 al., 2015). Following previous studies (O'Brien et al., 2003; Li et al., 2015), we incorporated the
- history of *Hp30* and *SME* indices by simply using their maximum values in the past 24 h and 3 h,
- respectively. The history lengths of the indices are not tested, and the alternative method of using
- mean values of the indices is not investigated. The model optimization requires significant work
- 450 efforts for an empirical model. However, the machine learning models inherently optimize the
- +30 chorts for an empirical model. However, the machine learning models innerently optimize the
- dependences of the model target on the parameters (Bortnik et al., 2016; Chu et al., 2017, 2021;
- 452 Huang et al., 2022; Ma, D., et al., 2022). The test of different empirical models could directly
- suggest the importance of each parameter, while the machine learning technique is more efficient in
- 454 providing the best model fit for many parameters.
- Our empirical models are developed using the Van Allen Probes data within 10° from the magnetic
- equator at L < 6.5. Additional data from the other spacecraft missions (THEMIS, Cluster, MMS, and
- 457 Arase) provide the waves and density measurements at higher L shells or higher latitudes. In this
- paper, the comparison between Van Allen Probes data and the model results is limited to latitudes
- within $\pm 10^{\circ}$. The chorus waves are confined close to the equator at the nightside, while the high
- powers of the dayside chorus are found at higher latitudes (Agapitov et al., 2018). A more
- 461 comprehensive wave model in L shell, MLT, and magnetic latitude is required to properly capture the

- high-latitude wave power. The evaluation of the model performance in other regions is left as a future
- 463 work.
- 464 Although the accuracy of the empirical models may be lower than the accuracy of machine learning
- 465 models, the empirical model inherently provides the average density and wave power under a certain
- 466 condition, which is stable and generally matches the data averaged over a sufficiently long period.
- The empirical model is robust if the data sampling time is sufficiently high in each category. The
- 468 empirical models of total electron density and whistler-mode wave power are applicable to radiation
- belt modeling on a timescale longer than several days (*Horne et al.*, 2013; *Glauert et al.*, 2014;
- 470 Drozdov et al., 2015), or under quiet to modestly disturbed geomagnetic conditions (Ma et al., 2015,
- 471 2017). During a short and disturbed period, the chorus and hiss wave amplitudes may be
- 472 underestimated, or the plume regions may be misidentified. Therefore, the wave model based on
- observation (Li et al., 2016b; Ma et al., 2018) or from machine learning prediction (Bortnik et al.,
- 474 2018) may provide better radiation belt modeling results. Our study of the empirical model
- 475 performance provides a reference for the future development of machine learning models, by
- 476 investigating the different error metrics and revealing the key factors affecting the model
- 477 performance.

478 **6 Conflict of Interest**

- 479 The authors declare that the research was conducted in the absence of any commercial or financial
- 480 relationships that could be construed as a potential conflict of interest.

481 7 Author Contributions

- Q.M. performed the surveys using satellite data, constructed the empirical models, made model-data
- 483 comparisons, evaluated the model performance, and wrote the manuscript. X.C., D.M. and S.H.
- 484 performed machine learning modeling, which helped inspire the evaluation methods for the
- performance of the empirical models, discussed the strengths and weaknesses of the empirical model,
- and revised the manuscript. W.L. and J.B. discussed the results of this project, suggested
- improvements to the models, revised the manuscript, and provided support for this project. X.S.
- 488 helped with the data preparation and global surveys, verified the data distribution, and revised the
- 489 manuscript.

490 8 Funding

- 491 This work is supported by NASA grants 80NSSC19K0911, 80NSSC20K0196, and
- 492 80NSSC22K1023. In addition, we acknowledge NASA grants 80NSSC19K0845 and
- 493 80NSSC20K0698, 80NSSC20K0704 and the NSF grants AGS-1847818 and AGS-2225445. SH
- 494 gratefully acknowledges the NASA FINESST grant 80NSSC21K1385. JB acknowledges support
- 495 from the Defense Advanced Research Projects Agency under the Department of the Interior award
- 496 D19AC00009.

497 **9** Acknowledgments

- We are grateful to the NASA and NSF agencies for their support of our research. The details of each
- 499 grant are listed in the 'Funding' section above.

500 10 Data Availability Statement

- The Van Allen Probes EMFISIS data are retrieved from http://emfisis.physics.uiowa.edu/Flight/, and
- 502 EFW data are retrieved from http://rbsp.space.umn.edu/data/rbsp/. The SuperMAG magnetic indices

- are retrieved from https://supermag.jhuapl.edu/mag/. The Hp30 index is retrieved from https://kp.gfz-
- 504 potsdam.de/en/hp30-hp60/data/. The empirical model and results of this paper are available in the
- data repository https://doi.org/10.6084/m9.figshare.22762247.

11 References

- 507 Agapitov, O., A. Artemyev, V. Krasnoselskikh, Y. V. Khotyaintsev, D. Mourenas, H. Breuillard, M.
- Balikhin, and G. Rolland (2013), Statistics of whistler-mode waves in the outer radiation belt:
- Cluster STAFF-SA measurements, J. Geophys. Res. Space Physics, 118, 3407-3420,
- 510 doi:10.1002/jgra.50312.
- Agapitov, O. V., Mourenas, D., Artemyev, A. V., Mozer, F. S., Hospodarsky, G., Bonnell, J., & V.,
- Krasnoselskikh (2018). Synthetic empirical chorus wave model from combined Van Allen
- Probes and Cluster statistics. Journal of Geophysical Research: Space Physics, 123, 297-314, doi:10.1002/2017JA024843.
- Bortnik, J., U. S. Inan, and T. F. Bell (2003), Frequency-time spectra of magnetospherically reflecting whistlers in the plasmasphere, J. Geophys. Res., 108(A1), 1030, doi:10.1029/2002JA009387.
- Bortnik, J., R. M. Thorne, and N. P. Meredith (2008), The unexpected origin of plasmaspheric hiss from discrete chorus emissions, Nature, 452, 62-66, doi:10.1038/nature06741.
- Bortnik, J., W. Li, R. M. Thorne, V. Angelopoulos, C. Cully, J. Bonnell, O. Le Contel, and A. Roux (2009), An observation linking the origin of plasmaspheric hiss to discrete chorus emissions, Science, 324(5928), 775, doi:10.1126/science.1171273.
- Bortnik, J., Li, W., Thorne, R. M., & Angelopoulos, V. (2016). A unified approach to inner magnetospheric state prediction. Journal of Geophysical Research: Space Physics, 121(3), 2423-2430. https://doi.org/10.1002/2015ja021733
- Bortnik, J., X. Chu, Q. Ma, W. Li, X. Zhang, R. M. Thorne, V. Angelopoulos, R. E. Denton, C. A. Kletzing, G. B. Hospodarsky, H. E. Spence, G. D. Reeves, S. G. Kanekal, and D. N. Baker (2018), Artificial neural networks for determining magnetospheric conditions, in: Machine
- 529 Learning Techniques for Space Weather, Elsevier, 279-300, doi:10.1016/b978-0-12-811788-530 0.00011-1.
- Breneman, A.W., Wygant, J.R., Tian, S. et al. (2022), The Van Allen Probes Electric Field and
 Waves Instrument: Science Results, Measurements, and Access to Data. Space Sci Rev 218, 69,
 https://doi.org/10.1007/s11214-022-00934-y.
- Carpenter, D. L., and R. R. Anderson (1992), An ISEE/whistler model of equatorial electron density in the magnetosphere, J. Geophys. Res., 97, 1097-1108.
- Chen, L., W. Li, J. Bortnik, and R. M. Thorne (2012a), Amplification of whistler-mode hiss inside the plasmasphere, Geophys. Res. Lett., 39, L08111, doi:10.1029/2012GL051488.
- Chen, L., Thorne, R. M., Li, W., Bortnik, J., Turner, D., and Angelopoulos, V. (2012b), Modulation
 of plasmaspheric hiss intensity by thermal plasma density structure, Geophys. Res. Lett., 39,
 L14103, doi:10.1029/2012GL052308.
- 541 Chen, L., et al. (2014), Generation of unusually low frequency plasmaspheric hiss, Geophys. Res. Lett., 41, 5702- 5709, doi:10.1002/2014GL060628.
- Chu, X., Bortnik, J., Li, W., Ma, Q., Denton, R., Yue, C., et al. (2017). A neural network model of three-dimensional dynamic electron density in the inner magnetosphere. Journal of Geophysical Research: Space Physics, 122(9), 9183- 9197. https://doi.org/10.1002/2017ja024464
- 546 Chu, X., Ma, D., Bortnik, J., Tobiska, W. K., Cruz, A., Bouwer, S. D., et al. (2021). Relativistic
- electron model in the outer radiation belt using a neural network approach. Space Weather, 19, e2021SW002808. https://doi.org/10.1029/2021SW002808

- 549 Drozdov, A. Y., Shprits, Y. Y., Orlova, K. G., Kellerman, A. C., Subbotin, D. A., Baker, D. N.,
- Spence, H. E., and Reeves, G. D. (2015), Energetic, relativistic, and ultrarelativistic electrons:
- Comparison of long-term VERB code simulations with Van Allen Probes measurements. J.
- Geophys. Res. Space Physics, 120, 3574- 3587. doi: 10.1002/2014JA020637.
- 553 Fu, X., et al. (2014), Whistler anisotropy instabilities as the source of banded chorus: Van Allen
- Probes observations and particle-in-cell simulations, J. Geophys. Res. Space Physics, 119, 8288-8298, doi:10.1002/2014JA020364.
- 556 Gjerloev, J. W. (2012), The SuperMAG data processing technique, J. Geophys. Res., 117, A09213,
 557 doi:10.1029/2012JA017683.
- Glauert, S. A., Horne, R. B., and Meredith, N. P. (2014), Three-dimensional electron radiation belt simulations using the BAS Radiation Belt Model with new diffusion models for chorus,
- plasmaspheric hiss, and lightning-generated whistlers, J. Geophys. Res. Space Physics, 119, 268-289, doi:10.1002/2013JA019281.
- Hartley, D. P., Cunningham, G. S., Ripoll, J.-F., Malaspina, D. M., Kasahara, Y., Miyoshi, Y., et al. (2023). Using Van Allen Probes and Arase observations to develop an empirical plasma density model in the inner zone. Journal of Geophysical Research: Space Physics, 128, e2022JA031012.
- Horne, R. B., S. A. Glauert, N. P. Meredith, D. Boscher, V. Maget, D. Heynderickx, and D. Pitchford (2013), Space weather impacts on satellites and forecasting the Earth's electron radiation belts with SPACECAST, Space Weather, 11, 169-186, doi:10.1002/swe.20023.
- Huang, S., Li, W., Shen, X.-C., Ma, Q., Chu, X., Ma, D., et al. (2022). Application of recurrent
 neural network to modeling Earth's global electron density. Journal of Geophysical Research:
 Space Physics, 127, e2022JA030695. https://doi.org/10.1029/2022JA030695
- Kasahara, Y., Miyoshi, Y., Omura, Y., Verkhoglyadova, O. P., Nagano, I., Kimura, I., and Tsurutani,
 B. T. (2009), Simultaneous satellite observations of VLF chorus, hot and relativistic electrons in
 a magnetic storm "recovery" phase, Geophys. Res. Lett., 36, L01106,
 doi:10.1029/2008GL036454.
- Kim, K., Lee, D. and Shprits, Y. (2015), Dependence of plasmaspheric hiss on solar wind parameters and geomagnetic activity and modeling of its global distribution. J. Geophys. Res. Space Physics, 120: 1153- 1167. doi: 10.1002/2014JA020687.
- Kim, K. C., & Shprits, Y. (2019). Statistical analysis of hiss waves in plasmaspheric plumes using
 Van Allen Probe observations. Journal of Geophysical Research: Space Physics, 124, 1904 1915. https://doi.org/10.1029/2018JA026458
- Kletzing, C. A., Kurth, W. S., Acuna, M., MacDowall, R. J., Torbert, R. B., Averkamp, T., Bodet, D.,
 Bounds, S. R., Chutter, M., Connerney, J. and Crawford, D. (2013), The Electric and Magnetic
 Field Instrument Suit and Integrated Science (EMFISIS) on RBSP, Space Sci. Rev.,
 doi:10.1007/s11214-013-9993-6.
- Kurth, W. S., De Pascuale, S., Faden, J. B., Kletzing, C. A., Hospodarsky, G. B., Thaller, S. and
 Wygant, J. R. (2015), Electron densities inferred from plasma wave spectra obtained by the
 Waves instrument on Van Allen Probes. J. Geophys. Res. Space Physics, 120, 904-914. doi:
 10.1002/2014JA020857.
- Li, W., Thorne, R. M., Meredith, N. P., Horne, R. B., Bortnik, J., Shprits, Y. Y., and Ni, B. (2008),
 Evaluation of whistler mode chorus amplification during an injection event observed on CRRES,
 J. Geophys. Res., 113, A09210, doi:10.1029/2008JA013129.
- Li, W., R. M. Thorne, V. Angelopoulos, J. Bortnik, C. M. Cully, B. Ni, O. LeContel, A. Roux, U. Auster, and W. Magnes (2009), Global distribution of whistler-mode chorus waves observed on the THEMIS spacecraft, Geophys. Res. Lett., 36, L09104, doi:10.1029/2009GL037595.
- Li, W., et al. (2013), An unusual enhancement of low-frequency plasmaspheric hiss in the outer plasmasphere associated with substorm-injected electrons, Geophys. Res. Lett., 40, 3798-3803, doi:10.1002/grl.50787.

- Li, W., Q. Ma, R. M. Thorne, J. Bortnik, C. A. Kletzing, W. S. Kurth, G. B. Hospodarsky, and Y.
- Nishimura (2015), Statistical properties of plasmaspheric hiss derived from Van Allen Probes
- data and their Effects on radiation belt electron dynamics, J. Geophys. Res. Space Physics, 120, doi:10.1002/2015JA021048.
- Li, W., O. Santolik, J. Bortnik, R. M. Thorne, C. A. Kletzing, W. S. Kurth, and G. B. Hospodarsky (2016a), New chorus wave properties near the equator from Van Allen Probes wave observations, Geophys. Res. Lett., 43, 4725-4735, doi:10.1002/2016GL068780.
- 605 Li, W., et al. (2016b), Radiation belt electron acceleration during the 17 March 2015 geomagnetic 606 storm: Observations and simulations, J. Geophys. Res. Space Physics, 121, 5520- 5536, 607 doi:10.1002/2016JA022400.
- Li, W., Shen, X. C., Ma, Q., Capannolo, L., Shi, R., Redmon, R. J., et al (2019), Quantification of
 Energetic Electron Precipitation Driven by Plume Whistler Mode Waves, Plasmaspheric Hiss,
 and Exohiss. Geophysical Research Letters, 46, doi:10.1029/2019GL082095
- Ma, D., Chu, X., Bortnik, J., Claudepierre, S. G., Tobiska, W. K., Cruz, A., et al. (2022). Modeling
 the dynamic variability of sub-relativistic outer radiation belt electron fluxes using machine
 learning. Space Weather, 20, e2022SW003079. https://doiorg.colorado.idm.oclc.org/10.1029/2022SW003079
- Ma, J., Gao, X., Chen, H., Tsurutani, B. T., Ke, Y., Chen, R., & Lu, Q. (2022). The effects of
 substorm injection of energetic electrons and enhanced solar wind ram pressure on whistler mode chorus waves: A statistical study. Journal of Geophysical Research: Space Physics, 127,
 e2022JA030502. https://doi.org/10.1029/2022JA030502.
- Ma, Q., B. Ni, X. Tao, and R. M. Thorne (2012), Evolution of the plasma sheet electron pitch angle distribution by whistler-mode chorus waves in non-dipole magnetic fields, Ann. Geophys., 30, 4, 751-760, doi:10.5194/angeo-30-751-2012.
- Ma, Q., W. Li, R. M. Thorne, B. Ni, C. A. Kletzing, W. S. Kurth, G. B. Hospodarsky, G. D. Reeves,
 M. G. Henderson, H. E. Spence, D. N. Baker, J. B. Blake, J. F. Fennell, S. G. Claudepierre, and
 V. Angelopoulos (2015), Modeling inward diffusion and slow decay of energetic electrons in the
 Earth's outer radiation belt, Geophys. Res. Lett., 42, 987-995. doi: 10.1002/2014GL062977.
- Ma, Q., W. Li, R. M. Thorne, J. Bortnik, G. D. Reeves, C. A. Kletzing, W. S. Kurth, G. B.
 Hospodarsky, H. E. Spence, D. N. Baker, J. B. Blake, J. F. Fennell, S. G. Claudepierre, and V.
 Angelopoulos (2016a), Characteristic energy range of electron scattering due to plasmaspheric
 hiss, J. Geophys, Res. Space Physics, 121, 11,737-11,749, doi:10.1002/2016JA023311.
- Ma, Q., et al. (2016b), Simulation of energy-dependent electron diffusion processes in the Earth's outer radiation belt, J. Geophys. Res. Space Physics, 121, 4217- 4231, doi:10.1002/2016JA022507.
- Ma, Q., Li, W., Thorne, R. M., Bortnik, J., Reeves, G. D., Spence, H. E., ... Baker, D. N. (2017).
 Diffusive transport of several hundred keV electrons in the Earth's slot region. Journal of
 Geophysical Research: Space Physics, 122, 10,235-10,246.
 https://doi.org/10.1002/2017JA024452
- Ma, Q., Li, W., Bortnik, J., Thorne, R. M., Chu, X., Ozeke, L. G., et al. (2018). Quantitative
 evaluation of radial diffusion and local acceleration processes during GEM challenge events.
 Journal of Geophysical Research: Space Physics, 123, 1938- 1952.
 https://doi.org/10.1002/2017JA025114.
- Ma, Q., Li, W., Zhang, X. -J., Bortnik, J., Shen, X. -C., Connor, H. K., et al. (2021). Global survey of
 electron precipitation due to hiss waves in the Earth's plasmasphere and plumes. Journal of
 Geophysical Research: Space Physics, 126, e2021JA029644.
 https://doi.org/10.1029/2021JA029644
- Malaspina, D. M., A. N. Jaynes, C. Boulé, J. Bortnik, S. A. Thaller, R. E. Ergun, C. A. Kletzing, and J. R. Wygant (2016), The distribution of plasmaspheric hiss wave power with respect to

- plasmapause location, Geophysical Research Letters, 43, 7878-7886, doi:10.1002/2016GL069982.
- Matzka, J., O. Bronkalla, G. Kervalishvili, J. Rauberg, Y. Yamazaki (2022), Geomagnetic Hpo index. V. 2.0. GFZ Data Services. https://doi.org/10.5880/Hpo.0002.
- Mauk, B. H., N. J. Fox, S. G. Kanekal, R. L. Kessel, D. G. Sibeck, and A. Ukhorskiy (2013), Science
 Objectives and Rationale for the Radiation Belt Storm Probes Mission, Space Sci. Rev., 1-15,
 doi:10.1007/s11214-012-9908-y.
- Meredith, N. P., Horne, R. B., Clilverd, M. A., Horsfall, D., Thorne, R. M., and Anderson, R. R.
 (2006), Origins of plasmaspheric hiss, J. Geophys. Res., 111, A09217,
 doi:10.1029/2006JA011707.
- Meredith, N. P., R. B. Horne, A. Sicard-Piet, D. Boscher, K. H. Yearby, W. Li, and R. M. Thorne
 (2012), Global model of lower band and upper band chorus from multiple satellite observations,
 J. Geophys. Res., 117, A10225, doi:10.1029/2012JA017978.
- Meredith, N. P., Horne, R. B., Kersten, T., Li, W., Bortnik, J., Sicard, A., & Yearby, K. H. (2018).
 Global model of plasmaspheric hiss from multiple satellite observations. Journal of Geophysical
 Research: Space Physics, 123, 4526- 4541. https://doi.org/10.1029/2018JA025226
- Meredith, N. P., Horne, R. B., Shen, X.-C., Li, W., & Bortnik, J. (2020). Global model of whistler
 mode chorus in the near-equatorial region (|λ_m|< 18°). Geophysical Research Letters, 47,
 e2020GL087311. https://doi.org/10.1029/2020GL087311
- Meredith, N. P., Bortnik, J., Horne, R. B., Li, W., & Shen, X.-C. (2021). Statistical investigation of
 the frequency dependence of the chorus source mechanism of plasmaspheric hiss. Geophysical
 Research Letters, 48, e2021GL092725.
- Morley, S. K., Brito, T. V., & Welling, D. T. (2018). Measures of model performance based on the log accuracy ratio. Space Weather, 16, 69-88. https://doi.org/10.1002/2017SW001669.
- Ni, B., J. Bortnik, R. M. Thorne, Q. Ma, and L. Chen (2013), Resonant scattering and resultant pitch angle evolution of relativistic electrons by plasmaspheric hiss, J. Geophys. Res. Space Physics, 118, 7740-7751, doi:10.1002/2013JA019260.
- O'Brien, T. P., and Moldwin, M. B. (2003), Empirical plasmapause models from magnetic indices, Geophys. Res. Lett., 30, 1152, doi:10.1029/2002GL016007, 4.
- Reeves, G., Spence, H. E., Henderson, M. G., Morley, S. K., Friedel, R. H. W., Funsten, H. O., et al. (2013). Electron acceleration in the heart of the Van Allen radiation belts. Science, 341(6149), 991-994. https://doi.org/10.1126/science.1237743.
- Reeves, G. D., R. H. W. Friedel, B. A. Larsen, R. M. Skoug, H. O. Funsten, S. G. Claudepierre, J. F. Fennell, D. L. Turner, M. H. Denton, H. E. Spence, J. B. Blake, and D. N. Baker (2016), Energy-dependent dynamics of keV to MeV electrons in the inner zone, outer zone, and slot regions, J. Geophys. Res. Space Physics, 121, 397-412, doi:10.1002/2015JA021569.
- Ripoll, J.-F., G. D. Reeves, G. S. Cunningham, V. Loridan, M. Denton, O. Santolík, W. S. Kurth, C. A. Kletzing, D. L. Turner, M. G. Henderson, and A. Y. Ukhorskiy (2016), Reproducing the observed energy-dependent structure of Earth's electron radiation belts during storm recovery with an event-specific diffusion model, Geophys. Res. Lett., 43, 5616-5625, doi:10.1002/2016GL068869.
- Santolík, O., M.Parrot, and F. Lefeuvre (2003), Singular value decomposition methods for wave propagation analysis, Radio Sci., 38(1), 1010, doi:10.1029/2000RS002523.
- Sheeley, B. W., M. B. Moldwin, H. K. Rassoul, and R. R. Anderson (2001), An empirical
 plasmasphere and trough density model: CRRES observations, J. Geophys. Res., 106(A11),
 25631-25641, doi:10.1029/2000JA000286.
- Shi, R., Li, W., Ma, Q., Green, A., Kletzing, C. A., Kurth, W. S., et al (2019). Properties of whistler mode waves in Earth's plasmasphere and plumes. Journal of Geophysical Research: Space Physics, 124. https://doi.org/10.1029/2018JA026041

- Sonwalkar, V. S., and Inan, U. S. (1989), Lightning as an embryonic source of VLF hiss, J. Geophys.
 Res., 94(A6), 6986-6994, doi:10.1029/JA094iA06p06986.
- Spasojevic, M., Shprits, Y. Y., and Orlova, K. (2015), Global empirical models of plasmaspheric hiss
 using Van Allen Probes, J. Geophys. Res. Space Physics, 120, 10,370-10,383,
 doi:10.1002/2015JA021803.
- Summers, D., Ni, B., and Meredith, N. P. (2007), Timescales for radiation belt electron acceleration and loss due to resonant wave-particle interactions: 2. Evaluation for VLF chorus, ELF hiss, and electromagnetic ion cyclotron waves, J. Geophys. Res., 112, A04207, doi:10.1029/2006JA011993.
- Summers, D., B. Ni, N. P. Meredith, R. B. Horne, R. M. Thorne, M. B. Moldwin, and R. R.
 Anderson (2008), Electron scattering by whistler-mode ELF hiss in plasmaspheric plumes, J.
 Geophys. Res., 113, A04219, doi:10.1029/2007JA012678.
- Tao, X., R. M. Thorne, W. Li, B. Ni, N. P. Meredith, and R. B. Horne (2011), Evolution of electron
 pitch angle distributions following injection from the plasma sheet, J. Geophys. Res., 116,
 A04229, doi:10.1029/2010JA016245.
- 711 Thorne, R. M., B. Ni, X. Tao, R. B. Horne, and N. P. Meredith (2010), Scattering by chorus waves as 712 the dominant cause of diffuse auroral precipitation, Nature, 467, 943-946, 713 doi:10.1038/nature09467.
- 714 Thorne, R. M. et al. (2013), Rapid local acceleration of relativistic radiation belt electrons by magnetospheric chorus, Nature, 504, 411-414, doi:10.1038/nature12889.
- 716 Thorne, R. M., J. Bortnik, W. Li, and Q. Ma (2021), Wave-particle interactions in the Earth's magnetosphere, doi:10.1002/9781119815624.ch6.
- Wygant, J.R., Bonnell, J.W., Goetz, K. et al. (2013), The Electric Field and Waves Instruments on
 the Radiation Belt Storm Probes Mission, Space Sci Rev 179, 183-220,
 https://doi.org/10.1007/s11214-013-0013-7
- Yue, C. Chen, L. Bortnik, J. Ma, Q. Thorne, R. M. Angelopoulos, V., ... Spence, H. E. (2017). The
 characteristic response of whistler mode waves to interplanetary shocks. Journal of Geophysical
 Research: Space Physics, 122, 10,047–10,057. https://doi.org/10.1002/2017JA024574
- Zhang, W., Ni, B., Huang, H., Summers, D., Fu, S., Xiang, Z., et al. (2019). Statistical properties of
 hiss in plasmaspheric plumes and associated scattering losses of radiation belt electrons.
 Geophysical Research Letters, 46, 5670- 5680. https://doi.org/10.1029/2018GL081863.
- Zhao, H., Ni, B., Li, X., Baker, D. N., Johnston, W. R., Zhang, W., Xiang, Z., Gu, X., Jaynes, A. N.,
 Kanekal, S. G., Blake, J. B., Claudepierre, S. G., Temerin, M. A., Funsten, H. O., Reeves, G. D.,
 & Boyd, A. J. (2019). Plasmaspheric hiss waves generate a reversed energy spectrum of
- radiation belt electrons. Nature Physics, 15(4), 367-372. https://doi.org/10.1038/s41567-018-0391-6.
- Zhou, C., et al. (2015), Excitation of dayside chorus waves due to magnetic field line compression in response to interplanetary shocks, J. Geophys. Res. Space Physics, 120,8327–8338, doi:10.1002/2015JA021530.

737

738

739

740

741

742743

744

745

746

Figure 1. Van Allen Probes observation and empirical modeling of the total electron density and whistler-mode chorus and hiss waves on 01 March 2013. (A) Geomagnetic Hp30 index and Hp*, which is the maximum Hp30 index during the previous 24 h; (B) geomagnetic SML index and SME*, which is the maximum SME index in the previous 3 h; (C) L shell and MLT of Van Allen Probe A; (D) total electron densities observed by Van Allen Probe A in the high-density plasmasphere or plume (blue) and in the low-density plasma trough (black), and produced by the empirical model (red); (E) magnetic power spectrogram at 20 Hz - 10 kHz frequencies observed by Van Allen Probe A, where the four white lines are equatorial electron gyrofrequency (f_{ce}), 0.5 f_{ce} , lower hybrid resonance frequency (f_{LH}), and proton gyrofrequency (f_{cp}); (F) chorus (black) and hiss (blue) wave amplitudes observed by Van Allen Probe A, and chorus (orange) and hiss (red) wave amplitudes produced from the empirical model. (G-J) Same as (C-F) except for the density and waves along the trajectory of Van Allen Probe B.

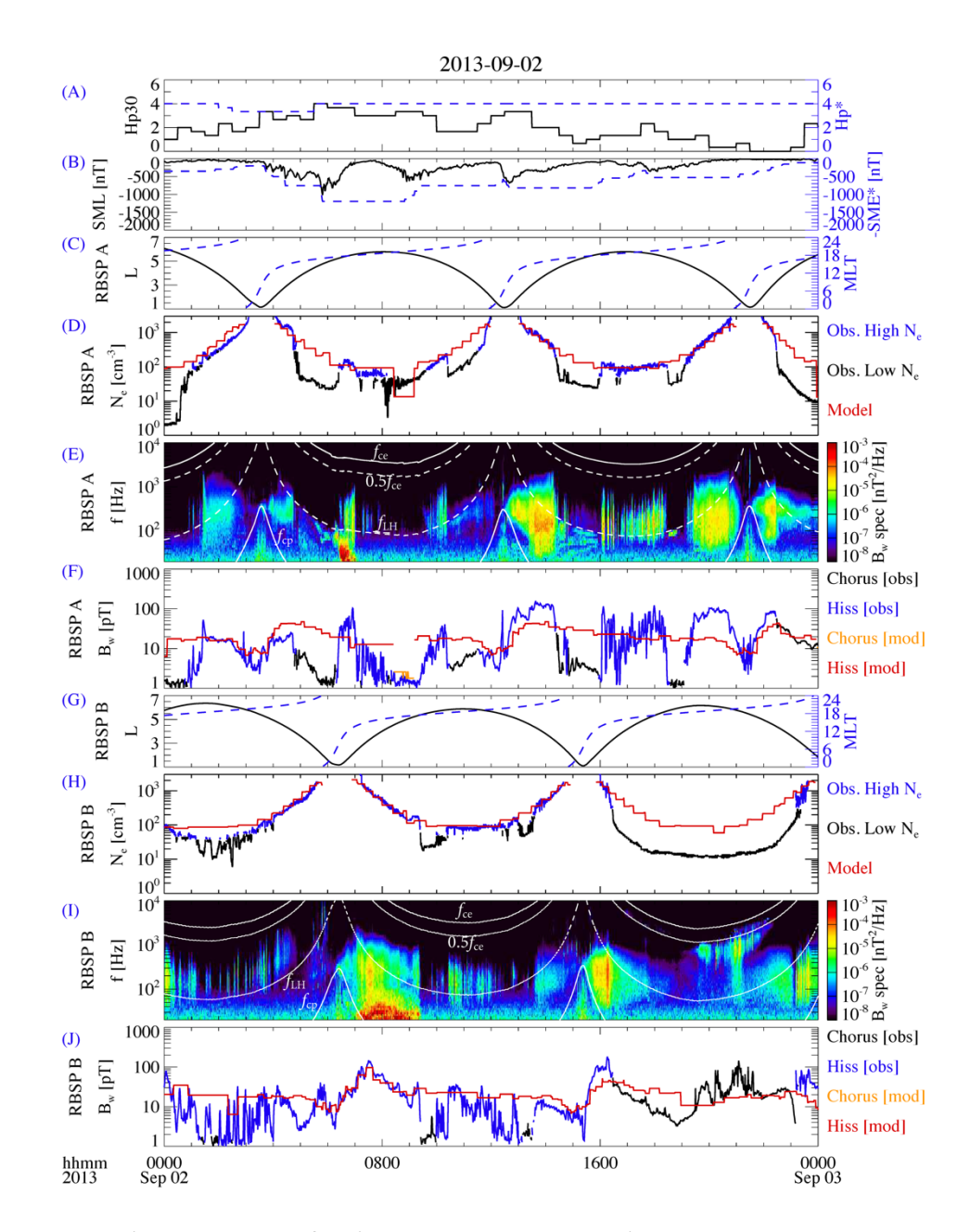


Figure 2. Same as Figure 2 except for the event on 02 September 2013.

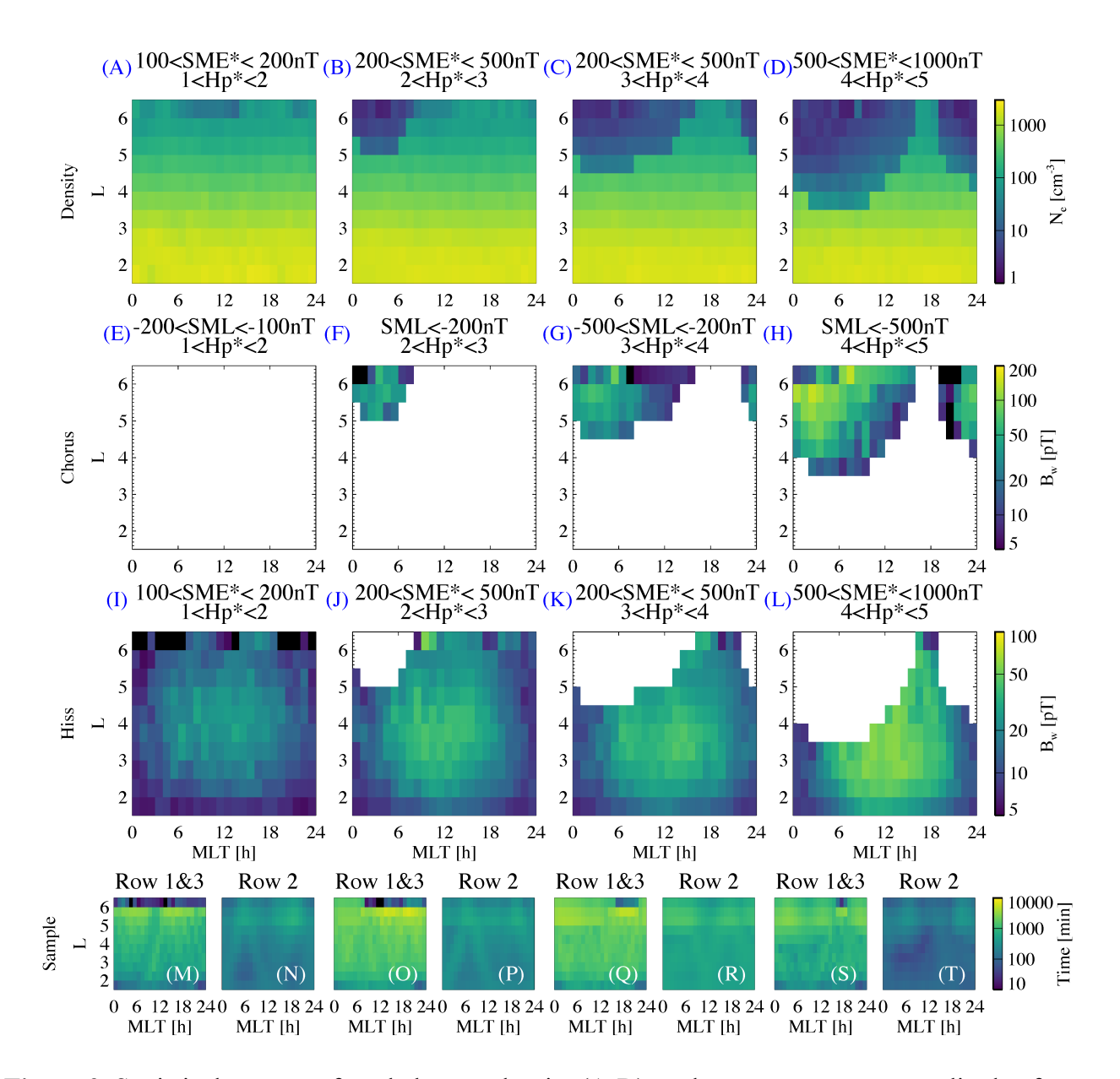


Figure 3. Statistical surveys of total electron density (A-D), and root-mean-square amplitude of chorus (E-H) and hiss (I-L) as a function of MLT and L shell, categorized by different Hp^* and SME^* or Hp^* and SML indices. (M) Total sample time under the geomagnetic condition for total electron density (Row 1, Panel A) or hiss (Row 3, Panel E), and (N) total sample time under the geomagnetic condition for chorus (Row 2, Panel E). (O-T) Same as (M-N) except for different geomagnetic conditions. Panels (E-H) only show the data in the region where the low-density occurrence rate is higher than the high-density occurrence rate; Panels (I-L) only show the data in the region where the high-density occurrence rate is higher.

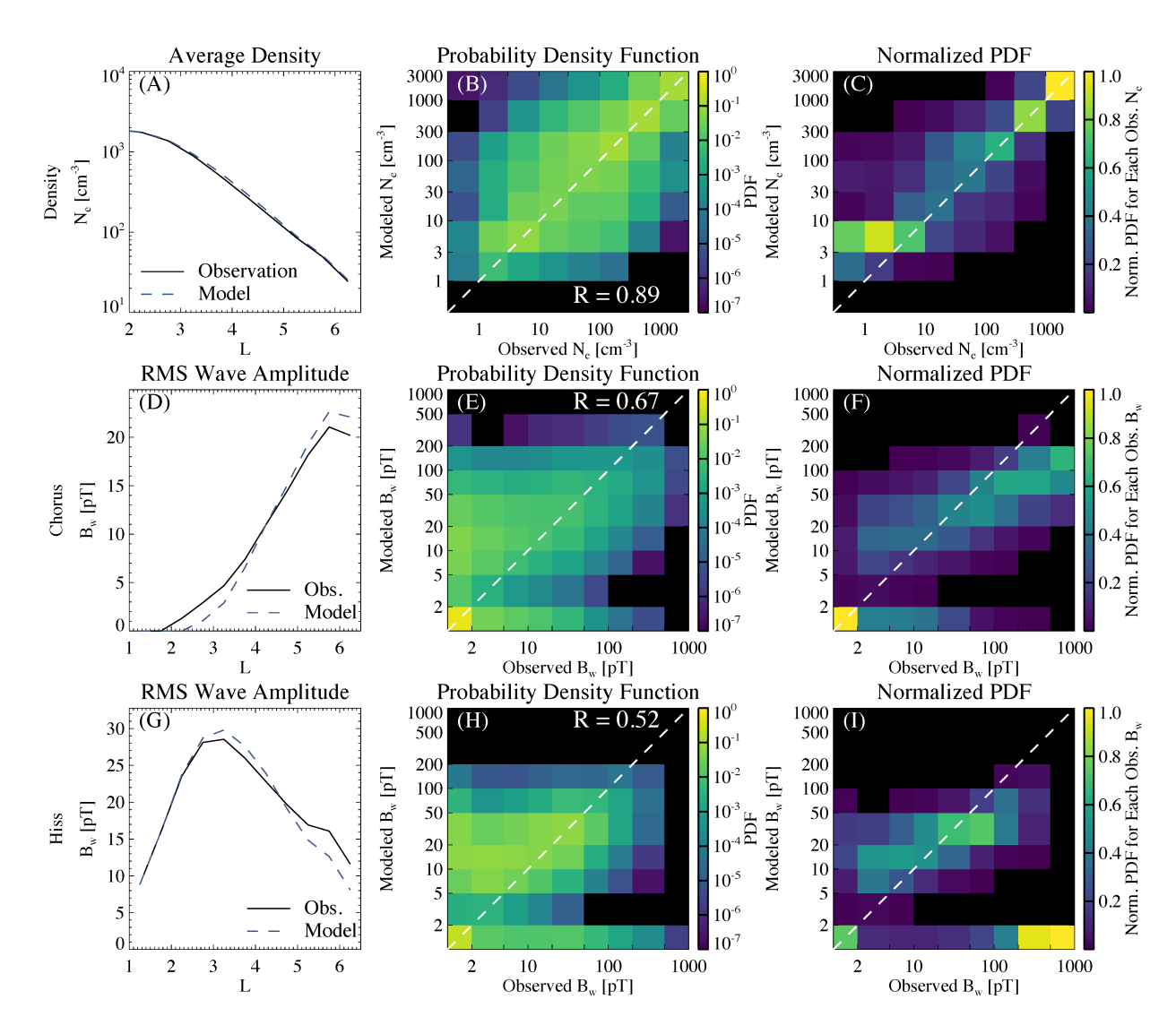


Figure 4. The comparison between observation and the empirical model, considering the Hp^* , SME^* index and modeled plasmapause for density and hiss, and considering the Hp^* , SML index and modeled plasmapause for chorus. (A) The average density as a function of L, where the solid and dashed lines are observation and modeling results, respectively; (B) probability density distribution as a function of modeled and observed densities; (C) probability densities divided by the total probability density within each bin of observed density. (D-F) Same as (A-C) except for the chorus wave amplitude. (G-I) Same as (A-C) except for the hiss wave amplitude.

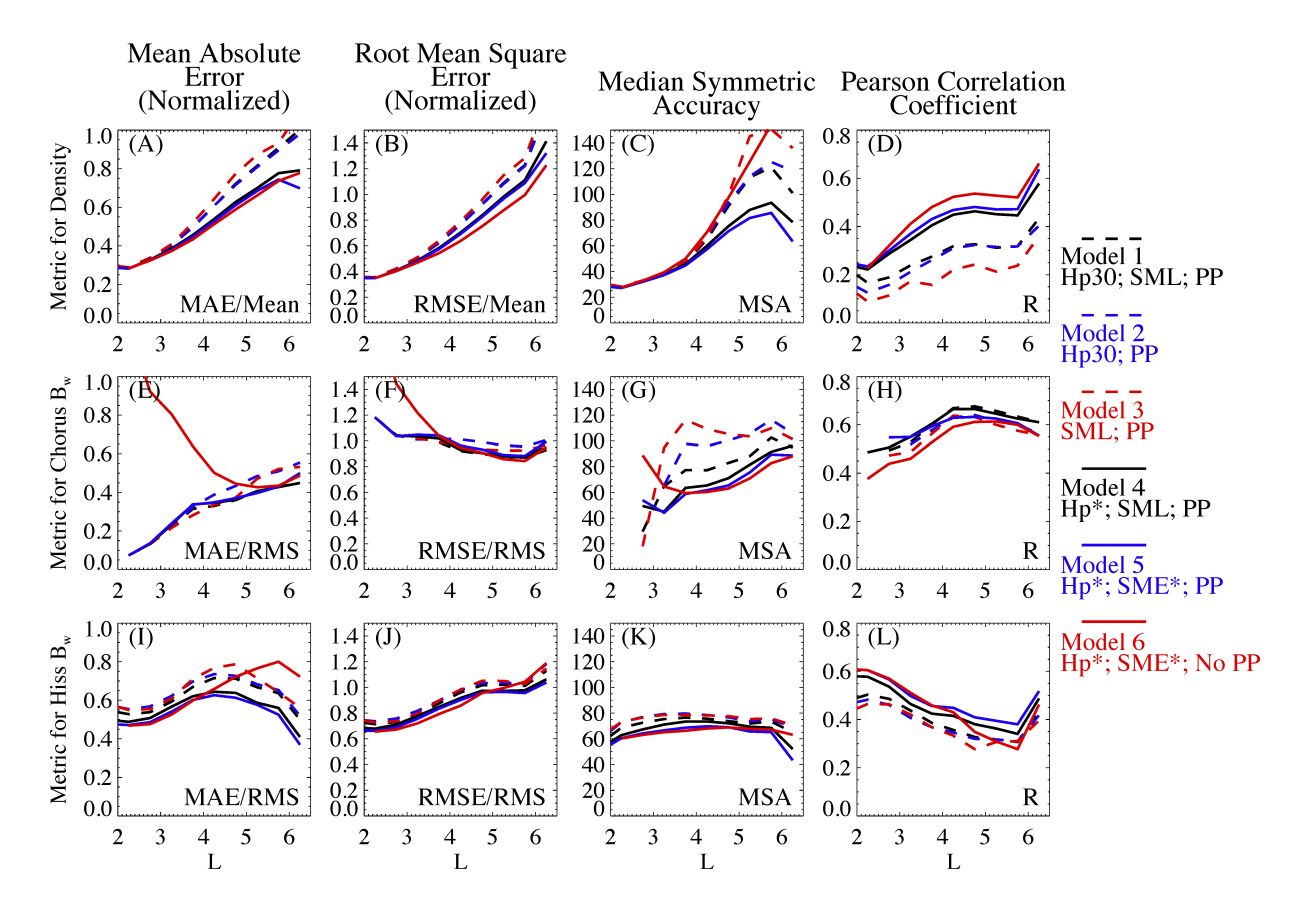


Figure 5. The performance of different empirical models evaluated using four metrics for different L shells. (A-D) Total electron density; (E-H) chorus wave amplitude; (I-L) hiss wave amplitude. The metrics include: Mean Absolute Error divided by the average of N_e or by the RMS B_w (chorus and hiss); Root Mean Square Error divided by the average of N_e or by the RMS B_w ; Median Symmetric Accuracy; Pearson Correlation Coefficient R. The different empirical models are illustrated by different line styles or colors.

Table 1. The overall performance of different empirical models evaluated using four metrics. The best performance evaluated by each metric is highlighted in bold blue font; the second best is highlighted in blue font; the worst performance is highlighted in bold black font.

Model	Mean Absolute Error			Root Mean Square Error			Median Symmetric Accuracy			Pearson Correlation Coefficient		
	MAE/Mean for N_e MAE/RMS for B_w			RMSE/Mean for N_e RMSE/RMS for B_w			MSA			R		
	Density $N_{ m e}$	Chorus $B_{ m w}$	Hiss $B_{ m w}$	Density $N_{ m e}$	Chorus $B_{ m w}$	Hiss $B_{ m w}$	Density $N_{ m e}$	Chorus $B_{ m w}$	Hiss $B_{ m w}$	Density $N_{ m e}$	Chorus $B_{ m w}$	Hiss $B_{ m w}$
Hp30, SML, PP	0.427	0.366	0.647	0.72	0.927	0.946	69.5	163	58.8	0.881	0.679	0.45
Hp30, PP	0.428	0.433	0.668	0.724	1.01	0.966	71.1	162	60.2	0.88	0.649	0.441
SML, PP	0.441	0.421	0.68	0.732	0.976	0.965	77.6	243	61	0.876	0.634	0.432
HP*, SML, PP	0.398	0.368	0.585	0.697	0.929	0.911	60.8	102	59.4	0.888	0.672	0.491
HP*, SME*, PP	0.393	0.369	0.562	0.691	0.945	0.894	57.8	104	57.1	0.89	0.653	0.517
HP*, SME*, No PP	0.401	0.451	0.682	0.702	0.926	0.908	84.3	89.3	51.8	0.888	0.637	0.475